J. Fluid Mech. (1981), *vol.* 111, *pp.* 175–195
Printed in Great Britain

A numerical study of rapidly rotating flow over surface-mounted obstacles

By P. J. MASON AND R. I. SYKES†
Meteorological Office, Bracknell, Berkshire

(Received 17 March 1979 and in revised form 26 January 1981)

Three-dimensional numerical integrations of the Navier–Stokes equations have been made for parameters corresponding to some previous laboratory studies of transverse flow past obstacles in a rotating fluid. In the laboratory experiments the character of the flow was found to depend upon the parameter $\mathscr{S}_L = L/DR$, where R is the Rossby number $U_0/\Omega L$, L is the horizontal scale of the obstacle, D the depth of the fluid, U_0 the flow speed and Ω the angular rate of rotation. For $\mathscr{S}_L \gg 1$ the flows appeared two-dimensional and our results confirm the applicability of this assumption in previous asymptotic theories. For $\mathscr{S}_L \sim 1$ a leaning disturbance is produced which can look columnar in character ('leaning Taylor column') and our results enable a detailed examination of this structure. To clarify the importance of nonlinear effects in the leaning Taylor column we compare them with the predictions of a linear inertial wave theory. This theory is valid only for small obstacle slopes but provided it includes the effects of viscosity it gives good predictions of the amplitude of the disturbances. The main difference between the viscous linear theory and the Navier–Stokes solution is a flow asymmetry of nonlinear origin. The role of viscosity is important but passive in the sense that it does not alter the flow structure near the obstacle but progressively dissipates the disturbance with increasing distance from the obstacle. This viscous confinement of the disturbance makes the lee wave flow structure look columnar and is important in allowing some laboratory flows to seem unbounded. The results also confirm the conjecture of Mason (1975, 1977) that the large drag forces occurring in these flows are due to inertial wave radiation.

1. Introduction

Previous work on transverse flow past obstacles in a rotating fluid has largely centred on the study of 'Taylor columns'. For sufficiently small values of Rossby number ($R = U/\Omega L$, where U is the flow speed, Ω the rotation speed and L a typical horizontal length) the rapid rotation constrains the motion about the obstacle to be two-dimensional (the Taylor–Proudman theorem: Proudman 1916; Taylor 1923). The flow past the object can then be divided into two regions separated by an imaginary cylinder with axis parallel to the axis of rotation, which circumscribes the object. Outside this cylinder (a 'Taylor column') the flow behaves as if it were encountering a solid cylinder. The exact conditions for a Taylor column to form have been discussed by Hide (1961) who proposed a criterion depending on the change in vorticity necessary for fluid filaments to cross the object, compared with the vorticity of the basic flow.

† Current address: Aeronautical Research Associates of Princeton, 50 Washington Road, Princeton, N.J. 08540.

It follows that a Taylor column should form when $\mathscr{S}_h = h/DR \gg 1$ (h is the height of the object and D the depth of the fluid). This is the criterion for virtually no flow over the obstacle and should be distinguished from the criterion for the flow to be nearly two-dimensional. The axial scale of a disturbance with horizontal scale L will be L/R and thus we require $\mathscr{S}_L = L/DR \gg 1$ for nearly two-dimensional motion.

Except for Stewartson & Cheng (1979) all the theoretical work in bounded systems (e.g. Jacobs 1964; Stewartson 1967; Ingersoll 1969) supposes $\mathscr{S}_L \gg 1$ but individual studies differ in the magnitude of $\mathscr{S}_h$ and whether or not viscous effects are included or even dominate. By assuming $\mathscr{S}_L \gg 1$ these studies exclude inertial wave radiation and have essentially two-dimensional solutions. Stewartson & Cheng consider inviscid flow for $\mathscr{S}_L = O(1)$ and obtain a solution with a bimodal structure, one part columnar and the other lee wave in character. In unbounded systems, previous studies have considered inviscid flow over shallow topography at arbitrary Rossby number (Queney 1947) or flow over ellipsoids at zero Rossby number (Grace 1926; Stewartson 1953). Both studies give waves radiating to infinity but the former has a lee wave structure whilst the latter is columnar.

In the laboratory experiments involving flow visualization the discussion of the results and data has centred on the 'Taylor-column' phenomenon. For $\mathscr{S}_h$ and $\mathscr{S}_L \gg 1$ these flows show Taylor-column disturbances extending parallel to the axis of rotation and in accordance with theoretical expectations they appear two-dimensional. When $\mathscr{S}_L$ and $\mathscr{S}_h$ are $O(1)$ the disturbance tilts with height and has been called a leaning Taylor column, see Hide & Ibbetson (1968) with an appendix by Lighthill (hereinafter both will be referred to as I). In the appendix Lighthill considers small-amplitude inertial waves far from the obstacle and obtains a value of the disturbance slope which agrees with experimental measurements near the obstacle. Stewartson & Cheng discuss this result and argue that, neglecting viscosity and nonlinearity, the disturbance would produce an extensive lee wave field complicated by the boundedness of the system. They compare their own $\mathscr{S}_L = O(1)$ solution with the leaning disturbances and conclude that a more detailed investigation of the structure of the disturbance with the aid of numerical solutions is necessary to determine the roles of nonlinear and viscous effects.

Also of relevance are previous laboratory experiments measuring the forces on obstacles moving horizontally in a rotating fluid (Mason 1975, 1977). In the parameter range $\mathscr{S}_L \sim 1$ a large drag force occurs of magnitude comparable to that expected from the radiation of inertial waves.

The main purpose of the present work is to provide more information on the nature of these leaning flow structures occurring when $\mathscr{S}_L \sim 1$. We present some three-dimensional integrations of the Navier–Stokes equations with parameters similar to those used in laboratory experiments. In contrast to previous three-dimensional integrations by Huppert & Bryan (1976) we consider smaller values of $\mathscr{S}_L$ at which the motion is distinctly three-dimensional. Our integrations enable the flow patterns to be seen in more detail than is possible in a laboratory experiment and the immediate impression is not of a tilting columnar disturbance but of a damped lee wave pattern extending away from the obstacle. To assist in interpreting the results we vary some parameters and make a comparison with the linear theory of Queney (1947) extended to take account of viscous effects.

Apart from the numerical results we also present some new laboratory experiments.

The original purpose of this comparison between numerical and laboratory experiments was to check that coding errors were absent from the numerics and that numerical errors were of the expected magnitude. In fact it did not prove possible to do this with useful accuracy owing to the limitations of the laboratory experiment. The experiment nevertheless provides confirmation that the numerical results are essentially correct.

In § 2 we outline the numerical model and indicate the ranges of accessible parameters. In § 3 we present the extension of Queney's (1947) theory to include viscous effects and in § 4 we describe the laboratory apparatus. In § 5 we present the results and finally in § 6 the conclusions.

2. Numerical model

The equations of motion governing the integrations reported in this paper are the Navier–Stokes equations for an incompressible rotating fluid, i.e.

$$\frac{\partial \mathbf{u}}{\partial t} + \mathbf{u} \cdot \nabla \mathbf{u} = -\nabla p + 2\boldsymbol{\Omega} \wedge (\mathbf{u} - \mathbf{u}_g) + \nu \nabla^2 \mathbf{u},$$

$$\nabla \cdot \mathbf{u} = 0,$$

where $\mathbf{u} = (u, v, w)$ is the velocity, p is the perturbation dynamic pressure, ν is the kinematic viscosity, and $\boldsymbol{\Omega}$ is the basic rotation. $\mathbf{u}_g = (U, 0, 0)$ is the geostrophic wind, resulting from the background pressure gradient in the y direction. The geometry and co-ordinate system are illustrated in figure 1. The boundary conditions on the upper and lower surfaces are

$$\frac{\partial u}{\partial z} = \frac{\partial v}{\partial z} = w = 0 \quad \text{on} \quad z = D$$

and

$$\mathbf{u} = 0 \quad \text{on} \quad z = h(x, y).$$

In both horizontal directions the domain of integration is taken to be periodic. The reason for this choice, apart from its numerical simplicity, is the desire to avoid either side-wall boundary layers requiring spatial resolution or the uncertainty in implementing inflow/outflow boundary conditions.

The numerical techniques we use to solve the equations have been discussed in Mason & Sykes (1978*a*, 1979) and will not be presented here. An important aspect of the numerical method concerns the approximate inclusion of the arbitrary no-slip surface $z = h(x, y)$. We use a Cartesian mesh and, in order for the method (which involves making the viscous stresses continuous at $z = h(x, y)$) to be effectively second-order accurate, certain resolution requirements must be met. For the flows considered here with Rossby number $R \lesssim 1$ the errors incurred near the surface are $O(\Delta/\delta)$ (Mason & Sykes 1978*a*), where Δ is the vertical mesh spacing and $\delta = (\nu/\Omega)^{\frac{1}{2}}$ is the depth of the Ekman boundary layer. In practice we find the results to be essentially independent of Δ/δ when $\Delta/\delta \lesssim \frac{1}{3}$. It follows that if, in the numerical model, we can dispose n grid points up to the height h_0 of the topography, then δ must be $\gtrsim 3h_0/n$. In the present work n may be about 20 giving $\delta \gtrsim h_0/7$. For Rossby numbers of unity and less this is the most stringent restriction on the model resolution. At larger Rossby numbers resolution is restricted by an upper limit to the Reynolds numbers which may be considered. For small-Rossby-number flows the restriction on δ/h_0 is only very

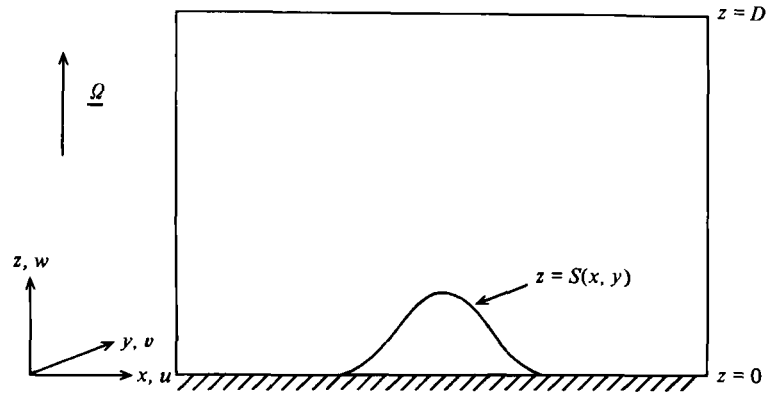

FIGURE 1. Illustrating the domain of the Navier–Stokes equation integrations.

severe for precisely those cases when a numerical model which parametrized the Ekman boundary layers (e.g. Vaziri & Boyer 1971) would be appropriate. In this paper some results are obtained slightly beyond the area of efficient application of the method in order to provide a check on the validity of the asymptotic assumptions involved in small-Rossby-number models.

3. Theoretical considerations

Here we consider small-Rossby-number flow and extend Queney's (1947) linear theory to include viscous effects. The linearized equations we are considering are

$$U_0\frac{\partial u}{\partial x}+fv=-\frac{\partial p}{\partial x}+\nu\nabla^2 u,$$

$$U_0\frac{\partial v}{\partial x}-fu=-\frac{\partial p}{\partial y}+\nu\nabla^2 v,$$

$$U_0\frac{\partial w}{\partial x}=-\frac{\partial p}{\partial z}+\nu\nabla^2 w,$$

$$\frac{\partial u}{\partial x}+\frac{\partial v}{\partial y}+\frac{\partial w}{\partial z}=0.$$

Since we are considering small-Rossby-number flow the lower boundary condition of Queney may be modified to include Ekman-boundary-layer pumping, i.e.

$$w=U_0\frac{\partial h}{\partial x}-\tfrac{1}{2}\delta\left(\frac{\partial v}{\partial x}-\frac{\partial u}{\partial y}\right) \quad \text{on} \quad z=0,$$

where $\delta=(2\nu/f)^{\frac{1}{2}}$ the Ekman-boundary-layer thickness. Solutions to Queney's inviscid problem show that for small Rossby number the vertical wavenumber associated with a horizontal x direction wavenumber k is $O(kR)$, where $R=U_0k/f$ is the Rossby number. It follows that, provided the Ekman number $E=\nu(k^2+l^2)/f$ (where l is a transverse horizontal wavenumber) is small enough to give a vertical decay scale larger than the horizontal wavelength we may neglect vertical derivatives in the viscous term. Thus instead of $\nu\nabla^2 u$ we have $\nu(\partial^2 u/\partial x^2+\partial^2 u/\partial y^2)$.

With this approximation, Fourier transformation of the equations with

$$h = \mathrm{Re}\{h_0 \exp[i(kx+ly)]\}$$

leads to solutions of the form $u = \mathrm{Re}\{u_0 \exp[i(kx+ly+mz)]\}$. If we maintain that $R^2 \ll 1$ and $E \ll 1$ we find

$$m = \frac{\lambda k U_0}{f} - \frac{i\nu\lambda^3}{f}$$

i.e.

$$m = \lambda R - i\lambda E,$$

where $\lambda = (k^2+l^2)^{\frac{1}{2}}$. Application of the boundary condition gives

$$w_0 = \frac{ikU_0h_0}{1+(\frac{1}{2}E)^{\frac{1}{2}}}, \qquad p_0 = \frac{-ikfU_0h_0}{\lambda(1+(\frac{1}{2}E)^{\frac{1}{2}})},$$

$$u_0 = iw_0\frac{k(R-iE)+l}{\lambda}, \qquad v_0 = iw_0\frac{l(R-iE)-k}{\lambda}.$$

It follows from the expressions for w_0 and p_0 that the wave drag on the surface though changed by the Ekman boundary layer, is unaltered by the internal dissipation. The full extent of the viscous effects depend on the exact numerical values of Ekman number and we postpone further discussion until § 5 where specific examples are presented.

In these examples we have sought specifically to compare with the results of our numerical integrations of the Navier–Stokes equations. As the Navier–Stokes equation model has, for reasons noted above, been taken as horizontally periodic we have avoided obtaining an analytic solution to the linear problem and have been able to obtain the desired results numerically. We have taken the size of the domain and the form of the topography to be exactly as in the Navier–Stokes integrations and have then used a uniform mesh of grid points to resolve the topography. A discrete fast Fourier transform was applied to the surface height field, and the required velocity fields were then numerically synthesized at the desired heights using the linear theory relations given above. A mesh of 64×64 grid points was used and from comparison with a test case of 128×128 grid points the results were judged essentially independent of resolution. Although this approach is very easy to implement the periodicity precludes us obtaining results comparable with analytic theories for isolated obstacles such as Stewartson & Cheng (1979).

4. Laboratory apparatus

The essential purpose of the apparatus was to tow an object mounted on a thin horizontal plate through a tank of fluid which was otherwise in solid body rotation. The fluid was contained in a rectangular tank mounted on a diameter of a turntable. The length of the tank was 1·20 m and the width and depth 0·20 m. The depth of the working fluid was generally less than the depth of the tank and the upper surface to the fluid was free. The axis of the turntable was vertical to within 10^{-4} radians and values of angular rotation speed Ω were in the range 0·5–1·0 rad s^{-1} and constant to within 0·01 %. The main errors in the experiment arose from spurious convection

	Case			
	A 1	A 2	A 3	B
Dimensional parameters				
Ω (rad s^{-1})	0·5	0·5	0·5	1·0
L (cm)	2	2	2	2
h_0 (cm)	2	1	2	1
D (cm)	20	20	20	3
U_0 (cm s^{-1})	0·2	0·2	0·2	0·1
ν (cm^2 s^{-1})	0·02	0 02	0·1	0·01
Dimensionless parameters				
$R = U_0/4\Omega L$	0·05	0·05	0·05	0·012
$E^{\frac{1}{2}} = (\nu/2\Omega D^2)^{\frac{1}{2}}$	$7{\cdot}1 \times 10^{-3}$	$7{\cdot}1 \times 10^{-3}$	$1{\cdot}6 \times 10^{-2}$	$2{\cdot}4 \times 10^{-2}$
$E^{\frac{1}{2}}/R$	0·14	0·14	0·31	1·19
$\mathscr{S}_h = h_0/DR$	2	1	2	27
$\mathscr{S}_L = L/DR$	2	2	2	53
$R_d = U_0 L/\nu$	20	20	4	20

TABLE 1. Basic parameters.

currents present in the fluid. These were minimized by extensive thermal insulation and the use of a thin film of oil on the upper surface of the fluid to prevent evaporation. The fluid was either water or, when a higher viscosity was desired, a water–glycerol mixture. The final magnitude of the background motions was $\simeq 0{\cdot}01$ cm s^{-1}. The thin horizontal plate had thickness 3 mm and was suspended from a framework by rods of 5 mm diameter mounted close to the edges of the tank. The objects used were sufficiently small for them to be effectively isolated from effects due to these rods and the sidewalls. The plate was long enough for the initial flow effects involving the formation of Ekman boundary layers to have subsided. This meant that the Rossby number based on the length of the plate had to be small. The other effect of the plate was a deflection of the flow through the mechanism of vortex compression (e.g. Batchelor 1967, p. 573). At smaller Rossby numbers than those for which data is presented, this effect necessitated the use of a thinner horizontal plate. As discussed in Mason (1975), effects due to the parabolic shape of the free upper surface of the liquid should be negligible.

The flow visualization was achieved by means of the well-known Baker (1966) technique employing the pH indicator thymol blue. Wires generating the pH change were attached to the framework supporting the horizontal plate and located upstream of the objects. Two 35 mm cameras were attached to the moving framework to photograph from above and from the side.

5. Results

In all the results presented, both numerical and experimental, we have adopted a standard form of topography. We have chosen a smoothly shaped obstacle to avoid both separation effects from sharp edges in the laboratory studies, and also numerical problems near sharp corners in the integrations. The height of the topography is

$$h = h_0 \cos^2\left[\frac{\pi}{2L}(x^2+y^2)^{\frac{1}{2}}\right] \quad \text{for} \quad x^2+y^2 < L^2,$$

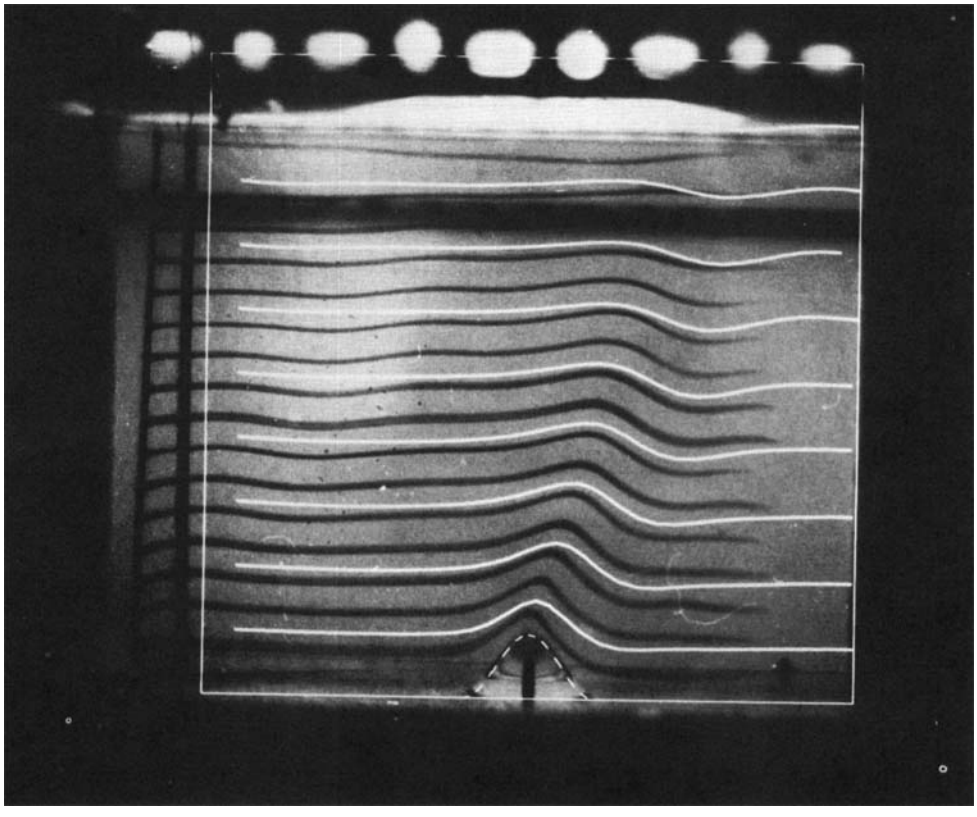

FIGURE 2. Superposition of experimental dye traces and computed trajectories from the numerical integration of case A 1 (see table 1).

$h = 0$ for $x^2+y^2 \geqslant L^2$. The relative size of the computational domain was $10L$ in the x-direction and $7{\cdot}5L$ in the y-direction. This was large enough to effectively isolate the topography.

(*a*) *Inertial-wave regime*

First we illustrate a flow typical of a so-called leaning Taylor column. A laboratory and a numerical experiment have been performed with the same basic parameters; these are given in table 1 case A 1. The Rossby number is small and $\mathscr{S}_L$, which is essentially the ratio of the vertical wavelength of the inertial waves to the depth of the container, is order unity. This and other parameters are typical of those used in previous experimental work such as I.

Figure 2 shows a comparison between the experimental dye observations and the numerical results. Starting at the upstream coordinates of the vertical dye-generation wire, trajectories have been computed from the steady-state numerical velocity field (by the method described in Mason & Sykes 1979) and superimposed onto a photograph of the experimental dye release. The comparison is difficult because although the initial co-ordinates are upstream of the centre of the obstacle in both sets of trajectories, small spurious motions in the experiment cause the dye to shift sideways slightly, into different parts of the velocity field, with consequent increasing errors. By calculating

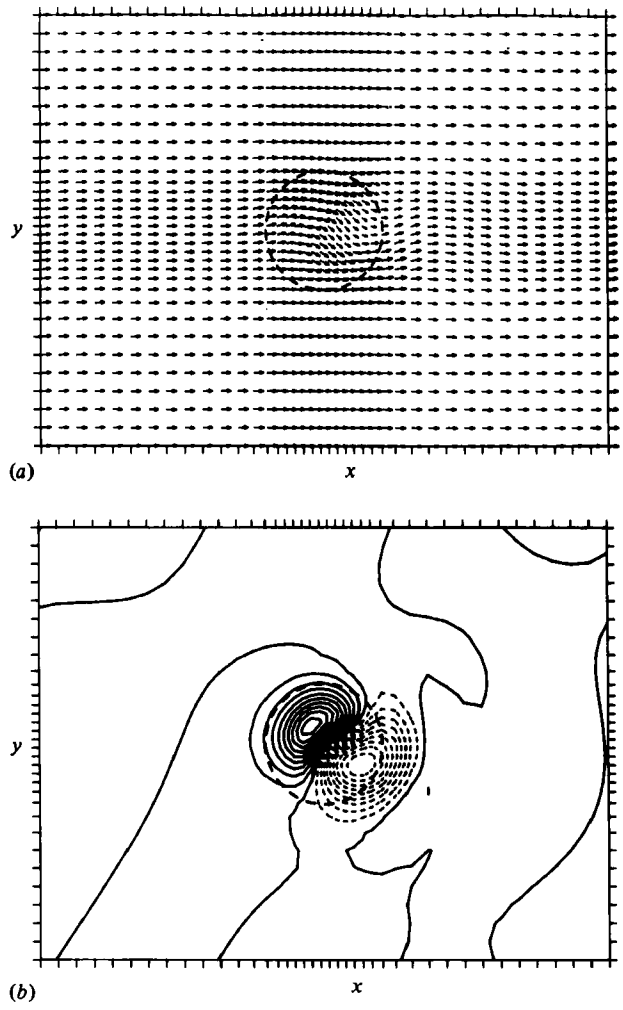

FIGURE 3(*a*, *b*). See caption on p. 183.

trajectories using the numerical results from different initial positions, it has been ascertained that errors due to the spurious lateral displacements in the laboratory study are typically of the same magnitude as the differences visible in the comparison. However it is clear that there is good agreement in the character of the flow. The disturbance is seen to decay both with height and in the downstream direction. With this type of flow visualization the lee wave character of the flow is fairly evident but in previous work such as I the dye sheets used did not give such a clear picture.

The example we have chosen has a slope of unity and a moderate amount of damping. To indicate the importance and role of nonlinearity and viscosity we have undertaken two further integrations in which only one parameter has been varied. In case A 2 we have reduced the height of the topography by a factor of two and in case A 3 we have increased the viscosity by a factor of five. As described in § 3 we have also undertaken linear theory calculations appropriate to these cases.

Rather than directly discuss the vertical variations of the flow seen in figure 2 we proceed with an inspection of some horizontal sections of the flow field. Firstly, in

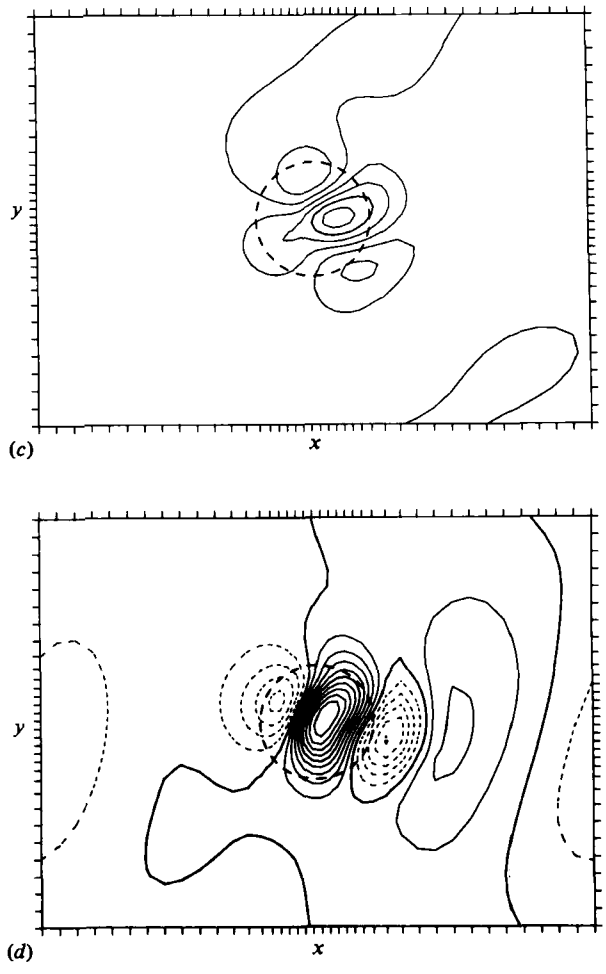

FIGURE 3. Results obtained from the numerical integration of case A 1. Horizontal sections at a height $z = h_0 + 3\delta$ where $\delta = (\nu/\Omega)^{\frac{1}{2}}$. (*a*) Horizontal velocity vectors. (*b*) Vertical velocity field. The contour interval is 0·015 cm s^{-1} and the dashed lines denote negative values. (*c*) Longitudinal velocity component. The contour interval is 0·02 cm s^{-1} and the undisturbed value in the field is 0·2 cm s^{-1}. The central feature is a minimum and the features either side maxima. (*d*) Transverse velocity component; note that owing to a plotting error the sign of this field has been reversed. The contour interval is 0·014 cm s^{-1} and dashed lines denote negative values.

figures 3 (*a–d*) we give a complete description of the flow field a few Ekman-layer depths above the top of the obstacle. Figure 3 (*a*) illustrates the significant deflection which occurs in the horizontal velocity flow vectors; the deflection is also evident in the vertical velocity field which is seen to be twisted out of alignment with the undisturbed flow. The peak magnitude of the vertical velocity is 0·15 cm s^{-1} and comparable with $u_0 \partial h_0/\partial x$. We thus conclude, in agreement with the implications of the trajectories in figure 2, that the vertical velocity at this level arises mainly from the observed horizontal flow vectors being displaced over the topography. Figure 3 (*c*) shows the longitudinal velocity field; this is quite different from that in a non-rotating flow and shows a minimum over the topography with maxima to the side. This structure follows from continuity considerations involving mainly the transverse velocities.

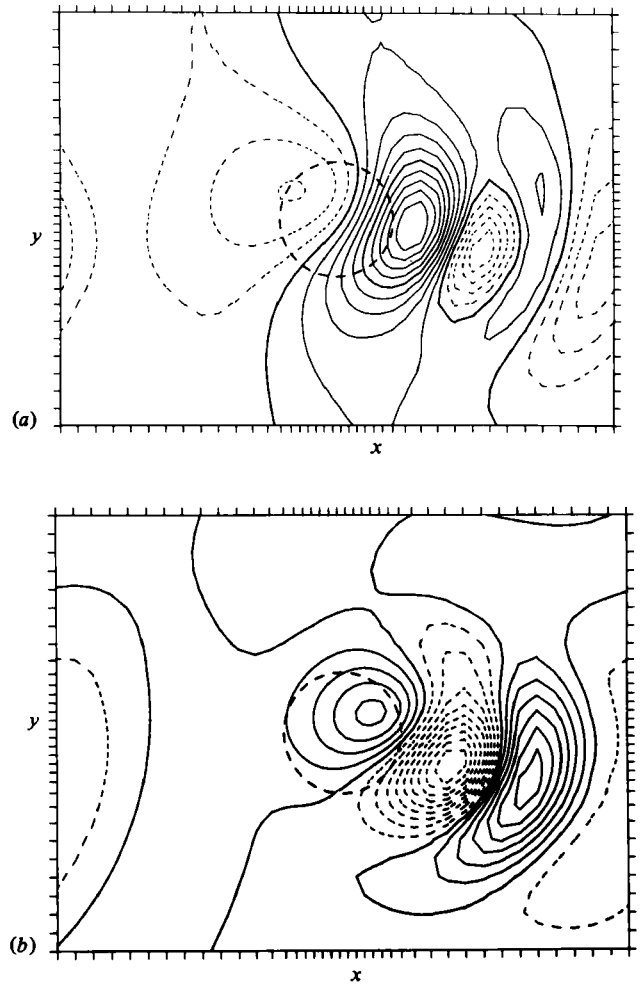

FIGURE 4. Results obtained from the numerical integration of case A 1. Horizontal sections at a height $z = \frac{1}{2}D$. (*a*) Transverse velocity component; note that owing to a plotting error the sign of this field has been reversed. The contour interval is 0·008 cm s^{-1}. (*b*) Vertical velocity component. The contour interval is 0·008 cm s^{-1}. Dashed lines denote negative values.

Over the topography the transverse velocity structure takes the form implied by vortex compression and subsequent expansion. As the flow ascends the topography, the vorticity $\partial v/\partial x$ is negative and as it descends $\partial v/\partial x$ is positive. Apart from this structure in the vicinity of the topography, other weak longer length scale features are evident in the rest of the domain. As we shall see below, these features appear to be a consequence of reflection from the upper boundary.

Figures 4(*a*, *b*) show horizontal sections of the transverse and vertical velocity components at $z = \frac{1}{2}D$. At this height the fields show the disturbances spreading and extending downstream in a wavelike fashion. The peak velocities are roughly half those occurring just above the topography. As before the fields contain weak features reflected from the upper boundary. Figures 5(*a*, *b*) show horizontal sections of the longitudinal and transverse velocity at $z = D$. Here of course the vertical velocity is

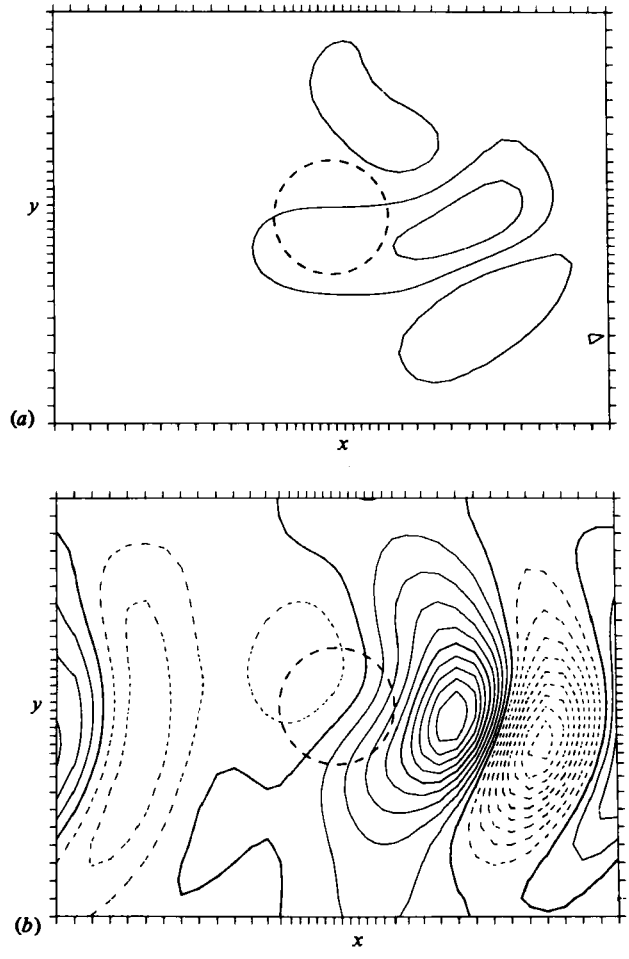

FIGURE 5. Results obtained from the numerical integration of case A 1. Horizontal sections at $z = D$. (*a*) Longitudinal velocity component. The contour interval is 0·02 cm s^{-1} and the undisturbed value in the field is 0·2 cm s^{-1}. The central feature is a minimum and the features to the side are maxima. (*b*) Transverse velocity component; note that owing to a plotting error the sign of this field has been reversed. The contour interval is 0·009 cm s^{-1}. Dashed lines denote negative values.

zero. The transverse velocity shows wavelike features, with wavelength roughly two obstacle diameters, extending around the domain. The longitudinal velocities take the form implied by continuity. The magnitude of the transverse velocity field is essentially the same as at $z = \frac{1}{2}D$ and it is these long length scale features which were seen, remote from the topography, in the fields at lower levels. The form of these weak long length scale disturbances is difficult to ascertain from sections involving the main topographic disturbance, and we thus present a longitudinal section one object diameter to the side of the base of the obstacle. Figure 6 illustrates the vertical velocity field in such a section taken on the side of the topography away from the flow deflection. The contour interval is 0·002 cm s^{-1} and indicates the small amount of energy present in motion on this scale. The flow structure clearly indicates that the motion is not two-dimensional and suggests a standing wave present in our domain.

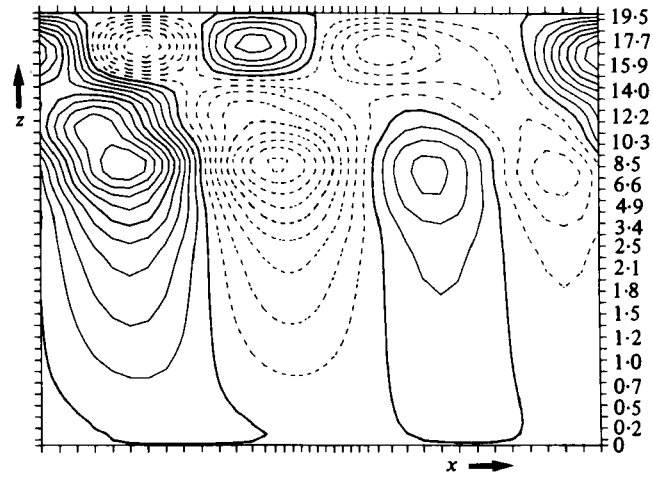

FIGURE 6. Results obtained from the numerical integration of case A 1. Vertical section in x, z plane of vertical velocity fields. The field is located at $y = +6$ cm, where $y = 0$ is at the centre of the topography. The contour interval is 0·002 cm s^{-1} and dashed lines denote negative values. Note that the vertical scale is non-uniform and corresponds with equal spacing in the computational mesh; actual heights are indicated.

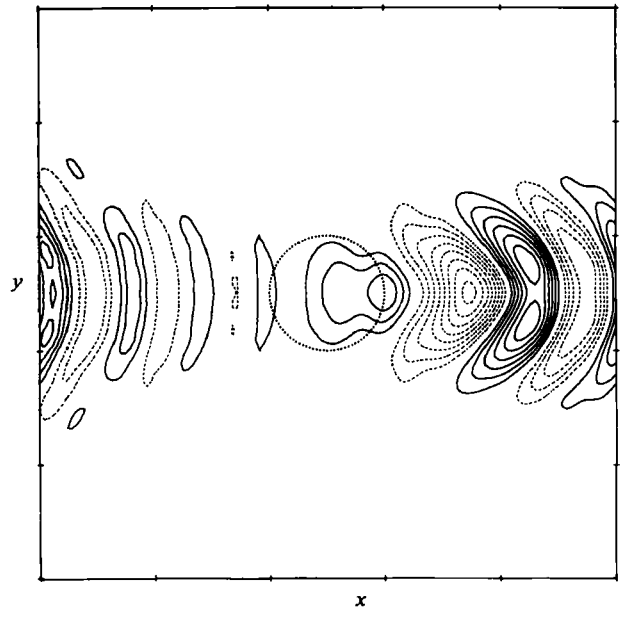

FIGURE 7. Results from inviscid linear theory for basic parameters corresponding to case A 1. A horizontal section of the vertical velocity field at a height $z = \frac{1}{2}D$ is shown. The contour interval is 0·02 cm s^{-1}.

The vertical wavenumber m associated with horizontal wavenumber was seen in § 3 to be $m = \lambda R$. If we consider the numbers involved in the present example we find that a wavelength of one object diameter, 4 cm, gives a wavenumber $k = 2\pi/4$ and Rossby number $R = u_0 k/f = 0{\cdot}3$. The vertical wavelength for such a mode is thus $\simeq \frac{1}{2}D$ and corresponds with the changes in structure with height which we have seen

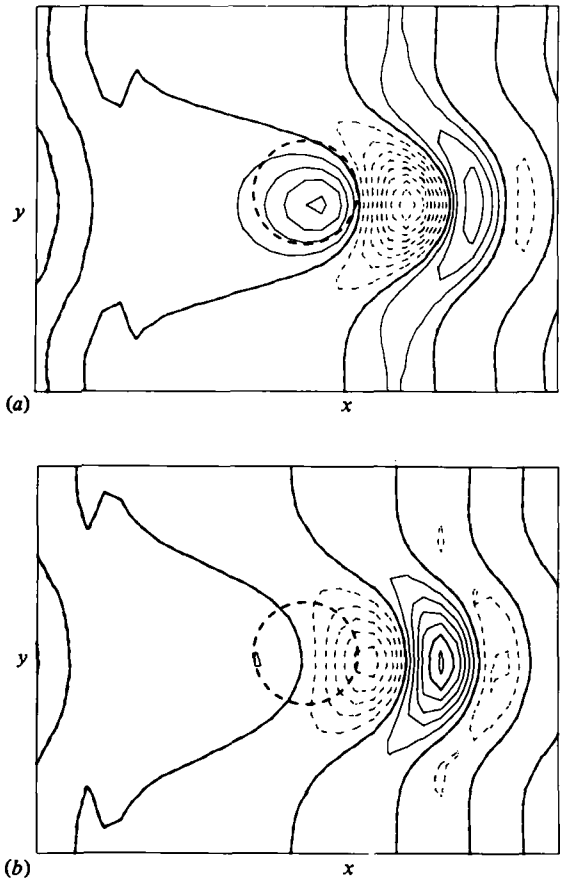

FIGURE 8. Results from viscous linear theory for case A 1 at a height $z = \frac{1}{2}D$. (*a*) Vertical velocity field. Contour interval 0·01 cm s^{-1}. (*b*) Transverse velocity field. Contour interval 0·01 cm s^{-1}.

in the main obstacle disturbance. For a scale of two object diameters, 8 cm, the Rossby number is $\simeq 0{\cdot}15$ and the vertical wavelength thus about $2D$. This is consistent with our observation of half a wavelength in a standing wave pattern. On longer scales we would expect the motion to be two-dimensional in form, with the vertical velocity decaying linearly with height from a value above the lower boundary layer to zero at $z = D$. However, in the examples we have considered the energy in such scales is too small to be separately identified.

We have taken the fields at $z = \frac{1}{2}D$ as convenient for a comparison with linear theory. In figure 7 we show the result of an *inviscid* calculation of the vertical velocity at this height. It is evident that at this height the periodicity of the domain is just beginning to affect the fields and many small-scale features are present. The peak velocity implied by the linear theory is twice that seen in the integrations but there is some similarity in the phase of the main features. In figures 8(*a*, *b*) we show the result of the viscous linear theory calculation. The vertical velocity field in figure 8(*a*) is quite different from the inviscid case; there is a small asymmetry and many small-scale features are removed. It should be compared with figure 4(*b*) which shows the result from the integration. The peak amplitude in the theoretical calculation is 0·08 cm s^{-1} and is

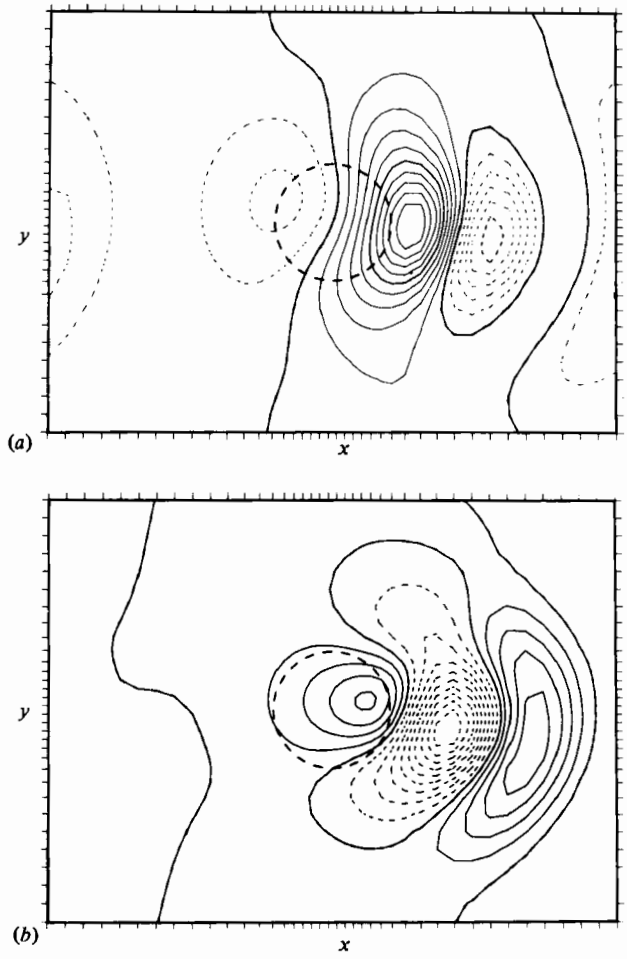

FIGURE 9. Results obtained from the numerical integration of case A 2. The topography has half the height of case A 1. Horizontal sections at $z = \frac{1}{2}D$. (*a*) Transverse velocity component; note that owing to a plotting error the sign of this field has been reversed. The contour interval is 0·0038 cm s^{-1}. (*b*) Vertical velocity component. The contour interval is 0·0036 cm s^{-1}. Dashed lines denote negative values.

in somewhat fortuitous exact agreement with the Navier–Stokes integration. The main differences are the large asymmetry and larger amplitude of the first downstream positive maximum in the integration. Differences between the transverse velocity field in the theory and in the integrations are of a similar character.

Although there are reflections from the top boundary the most likely cause of the differences, and the asymmetry in particular, is nonlinearity. We therefore conducted the integration A 2 with the topographic height halved but otherwise identical to case A 1. Figures 9(*a*, *b*) show the vertical velocity and transverse velocity fields for this integration (A 2) at the height $z = \frac{1}{2}D$. The flow is seen to be much closer to the linear theory; the asymmetry is reduced and relative magnitude of the features is closer. The peak amplitudes are roughly halved, maintaining agreement with linear theory. Weak, long length scale features reflected from the top boundary are still evident.

From these results we conclude that the flow structure contains significant non-linear effects. On the other hand the dominant dynamics, as revealed by the ability of linear theory to describe aspects of the flow, is that of inertial wave radiation. When linear theory is compared with the integrations at heights other than $z = \frac{1}{2}D$ it is found that below $z = \frac{1}{2}D$ agreement is as good or better than at $z = \frac{1}{2}D$, whilst above $z = \frac{1}{2}D$ agreement is less good. This is of course an inevitable and trivial result of comparing the bounded integrations with unbounded theory. The reason for the reasonable agreement up to $z = \frac{1}{2}D$ is simply that viscosity damps out most of the disturbance before it is reflected at the upper boundary. Without viscosity we would obtain a complex lee wave structure of the type described by Stewartson & Cheng (1979). We thus proceed to consider the role of viscosity in more detail.

In both the examples A 1 and A 2 the effect of viscosity is to reduce the amplitude of the disturbance at $z = \frac{1}{2}D$ to roughly one half of that near the lower boundary. Above $z = \frac{1}{2}D$ the transverse velocity amplitude is nearly independent of height, whilst the vertical velocity decays nearly linearly with height. In the viscous linear theory the decay rate decreases with height as longer wavelengths become dominant. We saw in § 3 that the rate of exponential decay of a particular wavenumber is λE, i.e. $\nu\lambda^3/f$ in dimensional terms. If we take the typical scale of the topography in the examples above, i.e. $\lambda = \pi/L$, we find $(f/\nu)\,\lambda^3 = 12{\cdot}9$ cm, i.e. $\simeq \frac{1}{2}D$. This is consistent with the form of the observed results but we must note the implication of the cubic scale dependence. A scale of $\frac{1}{2}L$ will be rapidly attenuated whilst a scale of $2L$ is hardly affected in the depth of our domain. It follows that the reflection of some energy from the upper boundary is difficult to avoid. Fourier analysis shows significant energy on the scale of our domain and implies that to effectively eliminate these reflections we would need a hundred-fold increase in either the depth or the viscosity. An increase in the horizontal size of the domain would not alter the extent of reflections but would help to distinguish upstream and downstream effects.

To provide confirmation of the ability of the viscous linear theory to account for the observed amplitudes, we have conducted a further numerical integration A 3. In this we have increased the viscosity of case A 1 by a factor of 5, other parameters remaining fixed. Figure 10 shows the resulting vertical velocity field at $z = \frac{1}{2}D$. The main differences from case A 1 are the increase in length scale of the disturbance and the reduction in amplitude by a factor of roughly three. Figure 11 shows the corresponding viscous linear theory result. The amplitude is still in good agreement and the differences including the asymmetry are much as with case A 1. Above $z = \frac{1}{2}D$ the behaviour is of the same character as in cases A 1 and A 2, but the motions roughly one third of the magnitude.

At this point we return to the question of the slope of the disturbances. Hide & Ibbetson (1968) measured the slope of the position of the maximum upward displacement of their dye sheet. This measurement was made near the obstacle and a value of $1{\cdot}54R$ (where $R = (u/\Omega)d$ and d is diameter of their sphere) was obtained. We made similar measurements *near* the obstacle and obtained a similar result. However as indicated in the discussion above, the vertical variation changes markedly with height becoming slight as $z = D$ is approached.

In this respect our numerical studies simply confirm Stewartson & Cheng's (1979) opinion that a complex lee wave pattern should result.

The above results show how, even though significant effects due to nonlinearity and

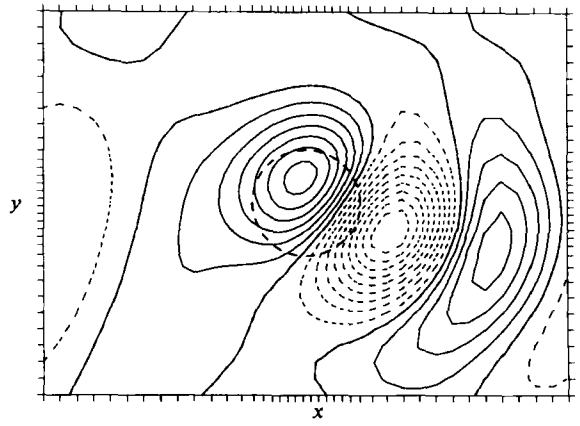

FIGURE 10. Results obtained from the numerical integration of case A 3. The viscosity is five times the value of case A 1. Horizontal section at $z = \frac{1}{2}D$ of the vertical velocity component. The contour interval is 0·0026 cm s^{-1} and dashed lines denote negative values.

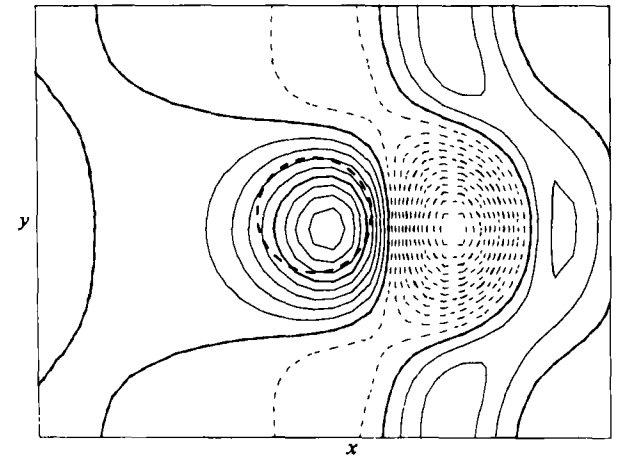

FIGURE 11. Results from viscous linear theory for the case A 3, vertical velocity component at $z = \frac{1}{2}D$. Contour interval 0·002 cm s^{-1} and dashed lines denote negative values.

boundedness are present, linearized unbounded inertial waves account for the dominant flow amplitudes and their phase variation with height. For this reason we would expect the perturbation pressure force arising from this wave radiation to accord with linear theory. This expectation is borne out in table 2 where drag forces from the numerical integrations and from linear theories are given. The linear theories only give a drag force in the basic flow direction and the viscous theory shows that Ekman boundary pumping reduces this drag. The internal dissipation had no effect on the drag given by the linear theory. In table 2 we see that for cases A 1 and A 2 the numerical integrations give small changes in viscous stress and the x direction drags compare favourably with linear theory. This is true even when the topographic slope is altered between cases A 1 and A 2. In the more nonlinear case A 1, the observed drag is smaller than the linear prediction. This result accords with experimental measurements of Mason (1975, 1977) and our observation of a wavelike structure confirms his conjecture that,

	Case			
	A 1	A 2	A 3	B
Undisturbed viscous force				
In x direction	$6{\cdot}53\times10^{-8}$	$6{\cdot}53\times10^{-8}$	$1{\cdot}40\times10^{-7}$	$3{\cdot}13\times10^{-8}$
In y direction	$5{\cdot}27\times10^{-8}$	$5{\cdot}27\times10^{-8}$	$1{\cdot}33\times10^{-7}$	$2{\cdot}88\times10^{-8}$
Final viscous force				
In x direction	$6{\cdot}48\times10^{-8}$	$6{\cdot}50\times10^{-8}$	$1{\cdot}36\times10^{-7}$	$3{\cdot}11\times10^{-8}$
In y direction	$5{\cdot}26\times10^{-8}$	$5{\cdot}27\times10^{-8}$	$1{\cdot}31\times10^{-7}$	$2{\cdot}85\times10^{-8}$
Perturbation pressure force on obstacle				
In x direction	$6{\cdot}0\times10^{-9}$	$2{\cdot}2\times10^{-9}$	$7{\cdot}3\times10^{-9}$	$2{\cdot}5\times10^{-9}$
In y direction	$3{\cdot}5\times10^{-9}$	$0{\cdot}4\times10^{-9}$	$1{\cdot}7\times10^{-9}$	$4{\cdot}9\times10^{-9}$
Calculated pressure force in x direction due to inviscid linearized inertial wave radiation	$8{\cdot}6\times10^{-9}$	$2{\cdot}2\times10^{-9}$	$8{\cdot}6\times10^{-9}$	—
Viscous linearized inertial wave radiation	$7{\cdot}5\times10^{-9}$	$1{\cdot}9\times10^{-9}$	$6{\cdot}4\times10^{-9}$	—
Perturbation pressure force on obstacle scaled by $2\Omega\rho U_0 v$				
In x direction	0·40	0·20	0·49	0·35
In y direction	0·23	0·04	0·11	0·68

TABLE 2. Net forces in MKS units

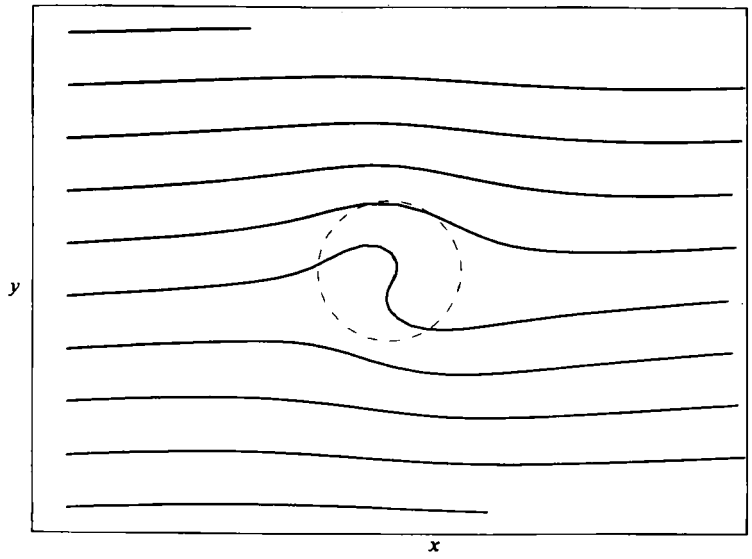

FIGURE 12. A projection onto a horizontal plane of computed flow trajectories at $z = \frac{1}{2}D$ in case B.

inertial wave radiation is the physical mechanism behind this drag. In accord with these experimental measurements but unlike the linear theory we also obtain a significant transverse force p_y. In case A 1 p_y is $\sim 0{\cdot}6p_x$ but in A 2 it is only $0{\cdot}18p_x$, strongly indicating a nonlinear origin related to the deflection of the undisturbed flow.

In case A 3 the Reynolds number is low enough to give significant viscous pressure

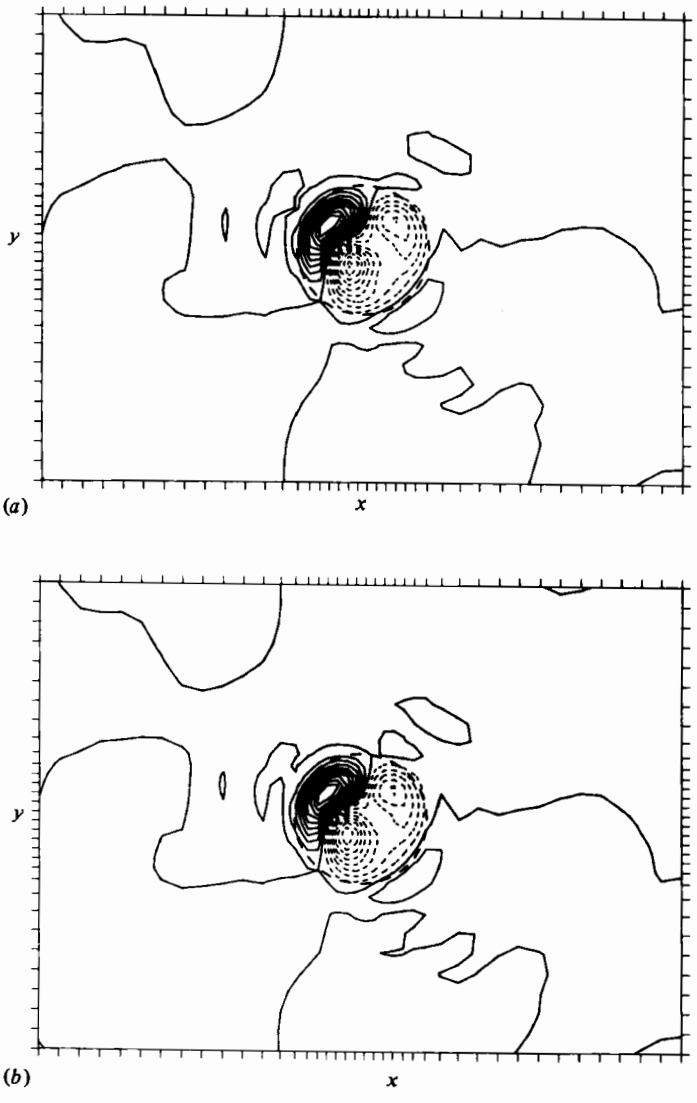

FIGURE 13. Results obtained from the numerical integration of case B. Horizontal sections of vertical velocity field at (*a*) $z = h_0 + 3\delta$ and (*b*) $z = \frac{3}{4}D$. The contour intervals are $1{\cdot}7 \times 10^{-3}$ and $0{\cdot}9 \times 10^{-3}$ cm s^{-1} respectively; dashed lines denote negative values.

effects and we cannot make definite statements regarding the forces obtained. The forces are however fairly consistent with those in cases A 1 and A 2.

(*b*) *Two-dimensional flow regime*

For comparison with the inertial wave flows, and as a check on the application of asymptotic theory, in this section we illustrate an example (*B*) of two-dimensional flows which occur when $\mathscr{S}_L \gg 1$. The parameters involved are given in table 1. In example *B*, viscous and inertial effects are comparable. The ratio of the spin-up time of the flow to the advection time $E^{\frac{1}{2}}/R = 1{\cdot}19$, cf. 0·14 in the inertial wave example A 1 in which internal dissipation was more important. For comparison with previous

results and with the experiments cited below, figure 12 shows a view from above of some flow trajectories at $z = \frac{1}{2}D$. It is clear that $\mathscr{S}_h$ is not large enough for the flow to be completely blocked but a strong deflection with much diminished flow above the obstacle is evident. Figures 13(*a*, *b*) show the vertical velocity fields just above the topography and at $z = \frac{3}{4}D$. The form of these fields is quite complex, reflecting the marked horizontal flow distortions. The two-dimensionality is seen to be fairly exact and even occurs in the zero contours which pick out weak features remote from the topography. This provides strong support for the use of asymptotic theory with $\mathscr{S}_L \gg 1$ at these parameters ($\mathscr{S}_L = 53$) and the form of our results accord with those of Vaziri & Boyer (1971) who have made a numerical study of these asymptotic equations.

In table 2 we present the forces arising in this integration. For a Taylor column with $\mathscr{S}_h \gg 1$ and $\mathscr{S}_L \gg 1$ theoretical expectations are for a transverse force equal to $2\Omega\rho u V$, where V is the volume of the topography. Here p_y is equal to 0·68 of this value and is consistent with the incomplete flow blocking. p_x is about half this value and probably due to Ekman-layer pumping (Mason & Sykes 1978*b*). Unfortunately theoretical estimates of drag due to this mechanism are only available for $\mathscr{S}_h \ll 1$ and we can only note that it is much less than the $\mathscr{S}_h \ll 1$ theory estimates.

6. Conclusions

We have shown the utility of a numerical model in studying rapidly rotating flow over topography. In an example with $\mathscr{S}_h = 27$ and $\mathscr{S}_L = 53$ we have confirmed that two-dimensional asymptotic theory is applicable. In another example with $\mathscr{S}_h = 2$ and $\mathscr{S}_L = 2$ we have considered flow typical of a laboratory experiment on 'leaning Taylor columns'. The complex flow at the later parameters shows a number of identifiable features.

The dominant part of the flow has the character of a lee wave system extending from the topography. Apart from a flow asymmetry the amplitude and phase of the disturbance are similar to those given by viscous linear theory. Such agreement would not be expected to hold for obstacles with greater slopes than the value of unity considered. The pronounced flow asymmetry reflects the large flow vector deflection and decreases when the obstacle slope is reduced.

For the parameters we have considered the flow is damped significantly by viscosity and the dominant flow structure occurs in the lower half of the domain. This accounts for Lighthill's successful prediction of the downstream tilt of the structure in the appendix to I using an unbounded wave radiation theory. The leaning structure is a spreading wave field rather than columnar. In the upper half of the domain the flow structure is strongly affected by the reflection from the upper boundary. This gives rise to a weak wave pattern filling the entire domain. A consideration of the scale dependence of the dissipation of inertial waves shows that such reflections are difficult to avoid in either laboratory or numerical studies. In the examples we have considered, the motions appear either entirely two-dimensional ($\mathscr{S}_L = 53$) or entirely wavelike ($\mathscr{S}_L = 2$). At intermediate parameters we would expect a structure exhibiting a basic two-dimensionality but with greater vertical variations than that seen in our $\mathscr{S}_L = 53$ example.

By showing that the $\mathscr{S}_L = \mathscr{S}_h = 2$ example was dominated by inertial waves we

have confirmed the conjecture (Mason 1975, 1977) that the drag forces at these parameters arise from inertial wave radiation.

Finally we note that we have shown that Stewartson & Cheng's (1979) conclusion that nonlinearity and viscosity are important in laboratory flows, is correct. However in spite of these effects, when examined in detail, the flows for $\mathscr{S}_L = O(1)$ do show features reminiscent of Stewartson & Cheng's solution. The 'column-like' part of their solution seems to correspond to the two-dimensional motion seen at $\mathscr{S}_L$ large and the wavelike part to the inertial waves we see at $\mathscr{S}_L \sim 1$. We can thus hypothesize that for an isolated obstacle in a less viscous system, the range of length scales affecting the flow would be larger, and both the two-dimensional and the wavelike parts would be simultaneously evident. To obtain such a flow it seems that less viscosity than that typical of either a laboratory system or our numerical integrations is needed.

The authors wish to express their gratitude to Mr W. D. N. Jackson who built the experimental apparatus and conducted the laboratory experiments. The authors are also grateful to Dr R. Hide for his support and to Dr M. E. McIntyre for stimulating discussions at the inception of the work.

REFERENCES

BAKER, D. J. 1966 A technique for the precise measurement of small fluid velocities. *J. Fluid Mech.* **26**, 573–576.

BATCHELOR, G. K. 1967 *An Introduction to Fluid Dynamics*. Cambridge University Press.

GRACE, S. F. 1926 On the motion of a sphere in a rotating liquid. *Proc. Roy. Soc.* A **113**, 46–47.

HIDE, R. 1961 Origin of Jupiter's Great Red Spot. *Nature* **190**, 213–218.

HIDE, R. & IBBETSON, A. 1968 On slow transverse flow past obstacles in a rapidly rotating fluid. *J. Fluid Mech.* **32**, 251–272.

HUPPERT, H. E. & BRYAN, R. 1976 Topographically generated eddies. *Deep Sea Res.* **23**, 655–679.

INGERSOLL, A. P. 1969 Inertial Taylor columns and Jupiter's Great Red Spot. *J. Atmos. Sci.* **26**, 744.

JACOBS, S. J. 1964 The Taylor column problem. *J. Fluid Mech.* **20**, 581–591.

LIGHTHILL, M. J. 1968 Theoretical considerations for the steady inviscid case with Rossby number small but not zero. Appendix to Hide & Ibbetson. *J. Fluid Mech.* **32**, 268–272.

MASON, P. J. 1975 Forces on bodies moving transversely through a rotating fluid. *J. Fluid Mech.* **71**, 577–599.

MASON, P. J. 1977 Forces on spheres moving horizontally in a rotating stratified fluid. *Geophys. Astrophys. Fluid Dyn.* **8**, 137–154.

MASON, P. J. & SYKES, R. I. 1978*a* A simple Cartesian model of boundary layer flow over topography. *J. Comp. Phys.* **28**, 198–210.

MASON, P. J. & SYKES, R. I. 1978*b* On the interaction of topography and Ekman boundary layer pumping in a stratified atmosphere. *Quart. J. Roy. Met. Soc.* **104**, 475–490.

MASON, P. J. & SYKES, R. I. 1979 Three-dimensional numerical integrations of the Navier–Stokes equations for flow over surface mounted obstacles. *J. Fluid Mech.* **91**, 433–451.

PROUDMAN, J. 1916 On the motions of solids in a liquid possessing vorticity. *Proc. Roy. Soc.* A **92**, 408–424.

QUENEY, P. 1947 The problem of air flow over mountains: a summary of theoretical studies. *Bull. Am. Met. Soc.* **29**, 16–26.

STEWARTSON, K. 1953 On the slow motion of an ellipsoid in a rotating fluid. *Quart. J. Mech. Appl. Math.* **6**, 141–162.

STEWARTSON, K. 1967 On slow transverse motion of a sphere through a rotating fluid. *J. Fluid Mech.* **30**, 357–363.

STEWARTSON, K. & CHENG, H. K. 1979 On the structure of inertial waves produced by an obstacle in a deep, rotating container. *J. Fluid Mech.* **91**, 415–432.

TAYLOR, G. I. 1923 Experiments on the motion of solid bodies in rotating fluids. *Proc. Roy. Soc.* A **104**, 213–218.

VAZIRI, A. & BOYER, D. L. 1971 Rotating flow over shallow topographies. *J. Fluid Mech.* **50**, 79–95.